2013

Penetration of UV-visible Solar Radiation in the Global Oceans: Insights from Ocean Color Remote Sensing

Zhongping Lee
University of Massachusetts Boston

Chuanmin Hu
University of South Florida, huc@usf.edu

Shaoling Shang
Xiamen University

Keping Du
School of Geography Beijing Normal University

Marlon Lewis
Dalhousie University

See next page for additional authors

JOURNAL OF GEOPHYSICAL RESEARCH: OCEANS, VOL. 118, 4241–4255, doi:10.1002/jgrc.20308, 2013

Penetration of UV-visible solar radiation in the global oceans: Insights from ocean color remote sensing

Zhongping Lee,[1] Chuanmin Hu,[2] Shaoling Shang,[3] Keping Du,[4] Marlon Lewis,[5] Robert Arnone,[6] and Robert Brewin[7]

Received 15 March 2013; revised 5 July 2013; accepted 9 July 2013; published 5 September 2013.

[1] Penetration of solar radiation in the ocean is determined by the attenuation coefficient ($K_d(\lambda)$). Following radiative transfer theory, K_d is a function of angular distribution of incident light and water's absorption and backscattering coefficients. Because these optical products are now generated routinely from satellite measurements, it is logical to evolve the empirical K_d to a semianalytical K_d that is not only spectrally flexible, but also the sun-angle effect is accounted for explicitly. Here, the semianalytical model developed in *Lee et al*. (2005b) is revised to account for the shift of phase function between molecular and particulate scattering from the short to long wavelengths. Further, using field data collected independently from oligotrophic ocean to coastal waters covering >99% of the K_d range for the global oceans, the semianalytically derived K_d was evaluated and found to agree with measured data within ~7–26%. The updated processing system was applied to MODIS measurements to reveal the penetration of UVA-visible radiation in the global oceans, where an empirical procedure to correct Raman effect was also included. The results indicated that the penetration of the blue-green radiation for most oceanic waters is ~30–40% deeper than the commonly used euphotic zone depth; and confirmed that at a depth of 50–70 m there is still ~10% of the surface UVA radiation (at 360 nm) in most oligotrophic waters. The results suggest a necessity to modify or expand the light attenuation product from satellite ocean-color measurements in order to be more applicable for studies of ocean physics and biogeochemistry.

Citation: Lee, Z., C. Hu, S. Shang, K. Du, M. Lewis, R. Arnone, and R. Brewin (2013), Penetration of UV-visible solar radiation in the global oceans: Insights from ocean color remote sensing, *J. Geophys. Res. Oceans*, *118*, 4241–4255, doi:10.1002/jgrc.20308.

1. Introduction

[2] Solar energy fuels life on Earth. In the ocean, solar irradiance is not only the driving force of photosynthesis and photobleaching processes [*Del Vecchio and Blough*, 2002; *Morel*, 1991; *Platt et al*., 1988; *Twardowski and Donaghay*, 2002] but also contributes to heat transfer in the ocean-atmosphere system [*Gnanadesikan et al*., 2010; *Jolliff et al*., 2012; *Kirk*, 1988; *Lewis et al*., 1990; *Morel and Antoine*, 1994; *Sathyendranath et al*., 1991; *Siegel et al*., 1995; *Zaneveld et al*., 1981]. Accurately quantifying the penetration of solar radiation from the surface to deeper waters is thus an important aspect in the study of ocean biology, physics, and biogeochemistry.

[3] Solar energy in the infrared is lost in the upper few meters due to the strong absorption of water molecules. The propagation of instantaneous solar radiation in the UV and visible domain, commonly measured as downwelling irradiance (E_d, w/m^2/nm), in the upper ocean column can be expressed as [*Mobley*, 1994]

$$E_d(\lambda, z) = E_d(\lambda, 0-)e^{-K_d(\lambda)z}, \quad (1)$$

where $E_d(\lambda, 0-)$ stands for spectral downwelling irradiance just below the surface and $K_d(\lambda)$ (m^{-1}) is the average spectral diffuse attenuation coefficient between the surface and depth (z, m) [*Austin and Petzold*, 1981; *Mueller and Trees*, 1997]. λ stands for wavelength (nm). Many years of study have resulted in models to accurately estimate $E_d(\lambda, 0-)$ based on solar elevation and atmospheric properties [*Gregg and Carder*, 1990; *Gueymard*, 2001]. Thus, the determination of $E_d(\lambda, z)$ in the global ocean is highly dependent on an accurate estimation of $K_d(\lambda)$. K_d is an apparent optical property (AOP) [*Preisendorfer*, 1976], and studies of radiative transfer in the oceans have found that $K_d(\lambda)$ is primarily a

[1]School for the Environment, University of Massachusetts Boston, Boston, Massachusetts, USA.
[2]College of Marine Science, University of South Florida, St. Petersburg, Florida, USA.
[3]State Key Laboratory of Marine Environmental Science, Xiamen University, Xiamen, China.
[4]State Key Laboratory of Remote Sensing Science, School of Geography, Beijing Normal University, Beijing, China.
[5]Department of Oceanography, Dalhousie University, Halifax, Nova Scotia, Canada.
[6]Department of Marine Science, University of Southern Mississippi, Stennis Space Center, Mississippi, USA.
[7]Plymouth Marine Laboratory, Plymouth, UK.

Corresponding author: Z. Lee, School for the Environment, University of Massachusetts Boston, Boston, MA 02125, USA. (zhongping.lee@umb.edu)

2169-9275/13/10.1002/jgrc.20308

function of the water's inherent optical properties (IOPs), solar elevation, and to a secondary degree the change of light field distribution with depth [*Berwald et al*., 1995; *Gordon*, 1989; *Kirk*, 1984; *Lee et al*., 2005b; *Preisendorfer*, 1976].

[4] To obtain a global observation of the diffuse attenuation coefficient, $K_d(490)$ is conventionally estimated through an empirical ratio of remote sensing reflectance (R_{rs}, sr^{-1}) at ~490 and ~555 nm [*Austin and Petzold*, 1981; *Mitchell and Kahru*, 1998; *Morel et al*., 2007c; *Mueller et al*., 2003; *Mueller and Trees*, 1997]. It is found that this approach generally works well for oceanic waters, but results in large errors (underestimation) in turbid coastal waters [*Darecki and Stramski*, 2004; *Jamet et al*., 2012; *Lee et al*., 2005a; *Mueller and Trees*, 1997; *Wang et al*., 2009]. In addition to this caveat, this approach generates K_d at 490 nm only, which is insufficient for the estimation of the spectral K_d that is required for a full account of the variation in the spectral distribution of light in the upper water column [*Sathyendranath and Platt*, 2007], although K_d at other discrete wavelengths could also be estimated through empirical approaches [*Fichot et al*., 2008; *Jamet et al*., 2012; *Johannessen et al*., 2003; *Loisel and Stramski*, 2000; *Smyth*, 2011], and a spectrum could be produced empirically from $K_d(490)$ [*Austin and Petzold*, 1986] or from empirically estimated chlorophyll concentration [*Morel and Maritorena*, 2001].

[5] Based on radiative transfer theory, relationships between K_d and the water's IOPs have also been developed [*Gordon*, 1989; *Kirk*, 1984], where $K_d(\lambda)$ can be expressed as an analytical function of the absorption ($a(\lambda)$, m^{-1}) and backscattering coefficients ($b_b(\lambda)$, m^{-1}) [*Lee et al*., 2005b],

$$K_d(\lambda) = (1 + m_0 \times \theta_s) \times a(\lambda) + \nu \times b_b(\lambda). \quad (2)$$

[6] Here, θ_s is the solar zenith angle above the sea surface in degrees. m_0 and ν are parameters deduced from the two-stream irradiance model [*Åas*, 1987], which were further empirically quantified with numerical simulations by Hydrolight [*Mobley*, 1995]. Because both $a(\lambda)$ and $b_b(\lambda)$ can be retrieved analytically or semianalytically from spectral $R_{rs}(\lambda)$ [*IOCCG*, 2006], K_d at any λ can then be calculated from $a(\lambda)$ and $b_b(\lambda)$. By explicitly incorporating sun angle in such models [also see *Kirk*, 1984; *Gordon*, 1989], the AOP nature of K_d is well revealed.

[7] In the development of the semianalytical K_d model (i.e., equation (2)) [*Lee et al*., 2005b], the shortest wavelength was limited to 400 nm, and the data set did not have a full representation of oligotrophic waters. As a result, equation (2) might not be accurate enough for K_d(UV) particularly in clear ocean waters. This is because for such clearer waters and for the shorter wavelengths, b_b is dominated by molecular scattering. Note that molecular scattering has a significantly different phase function compared to that of particle scattering [*Petzold*, 1972; *Sullivan and Twardowski*, 2009], which will thus contribute to AOPs differently [*Åas*, 1987; *Lee et al*., 2004; *Morel and Gentili*, 1991; *Sathyendranath and Platt*, 1997; *Stavn and Weidemann*, 1989]. On the other hand, knowledge of UV radiation penetration is important for the study of phytoplankton dynamics [*Gao et al*., 2012; *Hader et al*., 2007; *Smith and Cullen*, 1995], critical to quantify the photoreaction rates of dissolved organic matter (DOM) in the water column [*Kieber et al*., 1990; *Moran and Zepp*, 1997], and to understand coral bleaching in optically shallow waters [*Dunne and Brown*, 1996; *Lesser and Farrell*, 2004; *Shick et al*., 1996; *Sinha and Häder*, 2002; *Zepp et al*., 2008]. Therefore, it is necessary to revise equation (2) to account for this phase function effect in order to accurately estimate K_d from UV to the visible bands.

[8] The objective of this work is to refine the semianalytical K_d algorithm for waters ranging from the clearest oligotrophic ocean gyres to turbid coastal waters, including wavelengths in the UV and visible. We will first present the updated semianalytical K_d model based on Hydrolight simulations, and then evaluate the updated model using data measured in the clearest ocean waters as well as the ocean color data set compiled at the U.S. NASA by the Ocean Biology Processing Group (NASA bio-Optical Marine Algorithm Data set (NOMAD) data set). Finally, we apply the updated model to Moderate Resolution Imaging Spectroradiometer (MODIS) measurements of the global oceans to provide a global perspective of solar radiation penetration from the UVA to the visible bands.

2. Update of the Spectral K_d Model

[9] Following *Morel et al*. [2002], a parameter η_w is defined as

$$\eta_w(\lambda) = \frac{b_{bw}(\lambda)}{b_b(\lambda)}, \quad (3)$$

with b_{bw} for the backscattering coefficient of pure seawater. η_w thus provides a relative measure of the contribution of molecular backscattering to the total backscattering. Equation (2) is then revised by introducing a parameter γ to account for the effect of changing scattering agents

$$K_d(\lambda) = (1 + m_0 \times \theta_s) \times a(\lambda) + (1 - \gamma \times \eta_w(\lambda)) \times \nu \times b_b(\lambda). \quad (4)$$

[10] Further, we adopt the formula used in *Lee et al*. [2005b] to model parameter ν, and the final semianalytical expression for spectral K_d becomes

$$K_d(\lambda) = (1 + m_0 \times \theta_s) \times a(\lambda) + (1 - \gamma \times \eta_w(\lambda)) \times m_1 \times \left(1 - m_2 \times e^{-m_3 \times a(\lambda)}\right) \times b_b(\lambda). \quad (5)$$

[11] In this updated model, there are five parameters (γ and m_{0-3}) that need to be determined, and these model parameters are constants that do not vary with water properties or wavelengths.

[12] Hydrolight [*Mobley*, 1995] simulations were carried out to derive the values of the five model parameters in equation (5), and the simulations were focused on oligotrophic waters by setting chlorophyll-a concentrations (Chl) as 0.01, 0.02, 0.05, and 0.1 mg/m^3, along with the Case-1 bio-optical models of *Morel and Maritorena* [2001] for optical properties. Wavelengths were set in a range of 360–560 nm (20 nm step); water depth was set from 0 to 150 m (5 m step); and the Sun was positioned at 5°, 30°, and 60°, from zenith, respectively. Surface spectral irradiance was modeled with the Gregg and Carder model [*Gregg and Carder*, 1990], and wind speed was set as 5 m/s. No inelastic

Table 1. Model Parameters of the Revised Analytical K_d Model, Derived From Hydrolight Simulations

Parameters	Values
m_0	0.005
γ	0.265
m_1	4.259
m_2	0.52
m_3	10.8 m

scattering was included in these simulations as its contribution to downwelling irradiance is quite small in the UV-visible domain [*Morel and Gentili*, 2004]. From these simulations, as in *Lee et al*. [2005b], $K_d(\lambda)$ for the depth range between 0 m and the depth corresponding to 10% of the subsurface irradiance at the wavelength of interest was calculated, which was further used for the derivation of the model coefficients. To maintain continuity with the earlier K_d model and to achieve convergence when deriving model parameters, we kept the same values for m_0, m_2, and m_3, but let γ and m_1 vary; and they were further derived by nonlinear best fit. The final set of the derived model parameters are summarized in Table 1.

[13] To show the model performance, Figure 1a compares K_d from the updated model (equation (5) and Table 1) with Hydrolight-derived K_d for all low Chl values (<0.1 mg/m^3) and all wavelengths (255 points in total). Also shown in this figure is the performance of the *Lee et al*. [2005b] model (equation 2) to this data set, which shows an overestimation for nearly the entire K_d range. This is also manifested in Figure 1b where, for Chl = 0.02 mg/m^3, $K_d(\lambda)$ from Hydrolight and from the analytical models (equations 2 and 5) are compared to each other. To demonstrate the model continuity and consistency, Figure 1c shows the performance of the updated model to the data set used in *Lee et al*. [2005b]. The averaged absolute percentage difference between Hydrolight and the updated K_d model is 2.2% (slightly better than the $\sim$3% difference with equation 2) for both the 2005 data set and the simulated data set in this study, with a maximum absolute percentage difference as 9.8%. These statistic values indicate sufficient accuracy of the updated semianalytical model for a K_d range of $\sim$ 0.02–5.0 m^{-1}.

3. Retrieving a and b_b From R_{rs}

3.1. R_{rs} Model and Retrieval Algorithm

[14] The input variables to the updated K_d model are Sun angle, model parameters (Table 1), and IOPs, with the latter estimated from $R_{rs}(\lambda)$ through inversions [*IOCCG*, 2006]. As in *Lee et al*. [2010], because molecular scattering

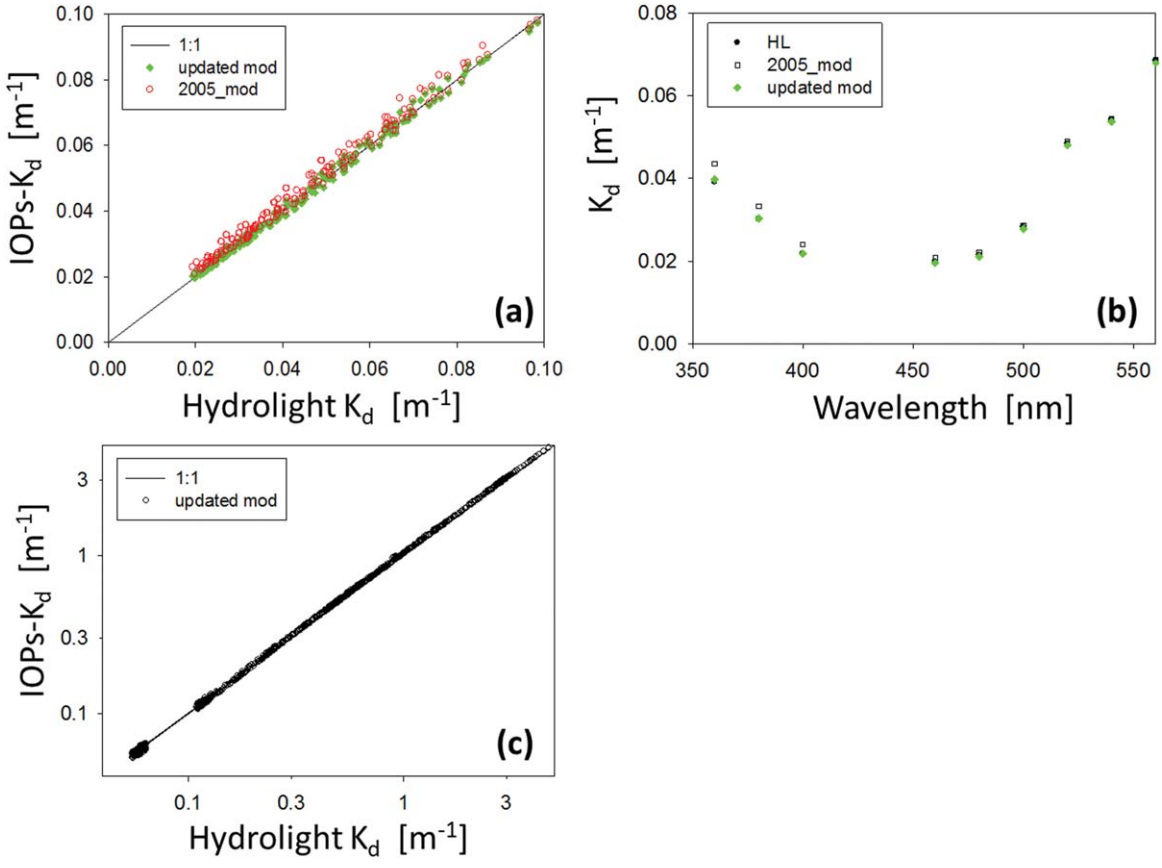

Figure 1. Comparison between Hydrolight-simulated K_d (HL) and semianalytically modeled K_d. (a) Performance of the updated model (green, from equation (5) and Table 1) and the 2005 model (red) for clear waters (266 points). (b) An example to show the improvement of the updated model (equation (5) and Table 1) from UVA to blue wavelengths. (c) Performance of the updated model to previous (2005, Sun at 30°) Hydrolight simulations.

makes the primary contribution to R_{rs} in the short wavelengths for oligotrophic waters, a R_{rs} model that explicitly separates the phase-function effects of molecular and particle scattering is used for the inversion:

$$R_{\mathrm{rs}}(\lambda,\Omega) = \left(G_0^w(\Omega) + G_1^w(\Omega)\frac{b_{\mathrm{bw}}(\lambda)}{\kappa(\lambda)}\right)\frac{b_{\mathrm{bw}}(\lambda)}{\kappa(\lambda)} + \left(G_0^p(\Omega) + G_1^p(\Omega)\frac{b_{\mathrm{bp}}(\lambda)}{\kappa(\lambda)}\right)\frac{b_{\mathrm{bp}}(\lambda)}{\kappa(\lambda)}, \quad (6)$$

with $\kappa = a + b_{\mathrm{b}}$ and $b_{\mathrm{b}} = b_{\mathrm{bw}} + b_{\mathrm{bp}}$, and b_{bp} is the backscattering coefficient of particles. Here Ω represents the Sun-sensor angular geometry for R_{rs}. Values of the model parameters $\left(G_0^w(\Omega), G_1^w(\Omega), G_0^p(\Omega), \text{and } G_1^p(\Omega);\ \mathrm{sr}^{-1}\right)$ for various Sun angles and viewing geometries have been developed based on Hydrolight simulations [*Lee et al*., 2011]. Their values are (0.0604, 0.0406, 0.0402, 0.1310 sr^{-1}) for nadir-viewed R_{rs}, and these values are applied in this study.

[15] For the retrieval of a and b_b from a given $R_{rs}(\lambda)$ spectrum, the quasi-analytical algorithm [*Lee et al*., 2002] (version 5; http://www.ioccg.org/groups/software.html) was used. Briefly,

[16] 1. 550 nm (for MODIS; it will be changed to 555 nm for Sea-viewing Wide Field-of-view Sensor (SeaWiFS), and 560 nm for Medium-Resolution Imaging Spectrometer (MERIS)) is selected as the reference wavelength (λ_0), and $a(\lambda_0)$ is estimated from

$$\begin{cases} \chi = \log\left(\dfrac{R_{rs}(443) + R_{rs}(490)}{R_{rs}(55\mathrm{x}) + 5\frac{R_{rs}(667)}{R_{rs}(490)}R_{rs}(667)}\right), & (7) \\ a(\lambda_0) = a_w(\lambda_0) + 10^{-1.146-1.366\chi-0.469\chi^2}, & (8) \end{cases}$$

with $a_w(\lambda_0)$, the absorption coefficient of pure water, taken from *Pope and Fry* [1997].

[17] 2. $b_{bp}(\lambda_0)$ is then calculated from the known $a(\lambda_0)$ and $R_{rs}(\lambda_0)$ with equation (6). To extrapolate $b_{bp}(\lambda_0)$ to the shorter wavelengths, spectral b_{bp} is described as

$$b_{bp}(\lambda) = b_{bp}(\lambda_0)\left(\frac{\lambda_0}{\lambda}\right)^Y. \quad (9)$$

[18] 3. Parameter Y is estimated from

$$Y = 2.0\left(1 - 1.2e^{-0.9\frac{R_{rs}(443)}{R_{rs}(55x)}}\right). \quad (10)$$

[19] The 55x represents 550, 555, and 560 nm for MODIS, SeaWiFS, and MERIS, respectively.

[20] 4. The total absorption coefficient for wavelength shorter than λ_0 is further calculated from the known spectral b_{bp} and spectral R_{rs} using equation (6).

[21] K_d values are then calculated by applying the above-derived IOPs and Table 1 to equation (5), with results termed as "IOPs-K_d" in this study.

3.2. Correction of the Raman-Scattering Effect

[22] For oligotrophic waters, Raman scattering could contribute 20% or more to R_{rs} for wavelengths longer than 550 nm [*Hu and Voss*, 1997; *Morel et al*., 2002; *Stavn and Weidemann*, 1988]. If R_{rs} in these wavelengths are used for IOPs retrievals (see section 3.1) without removing the Raman-scattering effect, a bias will be propagated into the derived properties [*Loisel and Stramski*, 2000]. Thus, a correction of the Raman-scattering effect is required in order to achieve a more realistic observation of the biooptical properties in oceanic waters.

[23] The estimation of the Raman-scattering contribution to R_{rs} requires knowledge of the IOPs at both the excitation and emission wavelengths [*Bartlett et al*., 1998; *Lee et al*., 1994; *Marshall and Smith*, 1990; *Westberry et al*., 2013]. This could be achieved semianalytically, and iteratively, by retrieving the a and b_{b} components using established algorithms [*Westberry et al*., 2013]. Here, as in *Lee et al*. [2010], for easier data processing, we employed an empirical approach for this correction. An empirical model to quantify the Raman Factor (RF) is developed as

$$RF(\lambda) = \alpha(\lambda)\left(\frac{R_{rs}^T(440)}{R_{rs}^T(550)}\right) + \beta_1(\lambda)\left(R_{rs}^T(550)\right)^{\beta_2(\lambda)}. \quad (11)$$

[24] Here, R_{rs}^T is the remote sensing reflectance that includes the Raman effect and is the value measured by all sensors; while RF is the ratio of the Raman-scattering induced remote-sensing reflectance $\left(R_{rs}^{Ra}\right)$ to the remote-sensing reflectance without contributions from Raman scattering (R_{rs})

$$RF = \frac{R_{rs}^{Ra}}{R_{rs}}. \quad (12)$$

[25] Then for any given R_{rs}^T from satellite or in situ measurements, the Raman effect corrected remote sensing reflectance is

$$R_{rs} = \frac{R_{rs}^T}{1 + RF}, \quad (13)$$

and this R_{rs} is used as the input for IOPs retrievals described in section 3.1.

[26] Equation (11) reflects that the Raman contribution decreases with increasing a (represented by the R_{rs} ratio and a positive α value) and increasing b_{b} (reflected by $R_{rs}(550)$, positive β_1 value and negative β_2 value). The model parameters in equation (11) (α, β_1, β_2) were derived from Hydrolight simulations and are presented in Table 2. The simulations used Chl values of 0.02, 0.05, 0.1, 0.2, 0.5, 1.0, and 3.0 $\mathrm{mg/m}^3$, along with the Case-1 biooptical model developed by *Morel and Maritorena* [2001]. Because the Raman effect is the strongest in clear oceanic waters that best follow the statistical Case-1 relationships [*Lee and Hu*, 2006], the simulation is considered valid for the correction of the Raman effect. The maximum relative difference between equation (11) modeled RF and Hydrolight derived RF is about 15%. Because the value of RF itself is small (generally less than 0.20), this model uncertainty (15% × 20% = 3%) has a negligible effect on the corrected R_{rs} (see equation 13).

[27] The Raman-scattering effect and model parameters are spectrally dependent. Table 2 presents the model

Table 2. Model Parameters for the Empirical Correction (equation (11)) of Raman-Scattering Contribution to the Measured R_{rs}, Derived from Hydrolight Simulations[a]

Wavelength	α	β_1	β_2
412	0.003	0.014	−0.022
443	0.004	0.015	−0.023
488	0.011	0.010	−0.051
531	0.015	0.010	−0.070
551	0.017	0.010	−0.080
667	0.018	0.010	−0.081

[a]Note that α and β_2 have no unit, β_1 has a unit associated with R_{rs}.

parameters for the MODIS visible bands, and a slight modification of these parameters could be applied to SeaWiFS and MERIS measurements. Note that there is no need for such a correction for empirical approaches (e.g., band ratio) to derive IOPs or chlorophyll concentrations [*Hu et al*., 2012; *O'Reilly et al*., 1998], as the empirical coefficients already include, implicitly, the Raman effects.

4. Data Sets Used to Evaluate Sensed K_d

[28] Two data sets, where K_d values were derived from the vertical profiles of $E_d(z)$ measurements, were used to evaluate the performance of the above described IOPs-K_d. The first is from the measurements during the Biogeochemistry and Optics South Pacific Experiment (BIOSOPE) (November 2004), where 24 spectral K_d (350–700 nm, 2 nm interval) that include the clearest natural waters were measured; the second is the NOMAD data set ($N > \sim$1500) with data collected from various parts of the global oceans, with K_d at 412, 443, 490, and 510 nm. Detailed description of the data collection and processing can be found in *Werdell and Bailey* [2005], and both data sets are collectively termed as "profile-K_d" in this presentation.

[29] For the BIOSOPE data, K_d was estimated at 1 m intervals based on depth profiles of the downwelling spectral E_d, measured at 3.3 nm increments from 350 to 700 nm with a wavelength accuracy of ±0.1 nm [*Gordon et al*., 2009]. The measurements were obtained using a free-fall profiling radiometer system (HyperPro II, Satlantic Inc.). Sensors were characterized and calibrated with standards traceable to National Institute for Standards and Technology (NIST); absolute radiometric uncertainty is assessed at <2.1% for irradiance [*Gordon et al*., 2009]. Dark corrections are made using an internal optical shutter operated throughout each profile. An above-water downwelling irradiance sensor mounted in the ship's superstructure is used to ensure stable surface values as the profile is taken, and tilt and temperature measurements are made using sensors onboard the instrument. Quality control procedures include elimination of data with instrument tilts >5°, and any profiles with significant fluctuations in surface irradiance due to clouds. Data from the radiance and irradiance sensors are then interpolated to common depth and wavelength bins and referenced to absolute depth by way of surface pressure tare values.

[30] To obtain K_d for the upper-water column to match K_d of equations (2) and (5), a depth weighted mean K_d was calculated following *Gordon and Clark* [1980],

$$\langle K_d \rangle = \frac{\int_0^{Z_d} K_d(z) W(z) dz}{\int_0^{Z_d} W(z) dz}, \tag{14}$$

with $W(z)$ being the weighting factor that decreases exponentially with increasing depth:

$$W(z) = e^{-2\int_0^Z K_{d(z)dz}}. \tag{15}$$

[31] Z_d in equation (14) represents the thickness of the surface layer and was taken as 80 m, which is deeper than the depth where 90% of upwelling light originates [*Gordon and Mcluney*, 1975]. There are four stations where K_d just below the surface (0–4 m) was either negative or close to 0 m^{-1}. These data were not included in the calculation of $<K_d>$. Furthermore, the evaluation of K_d was limited for wavelengths between 350 and 550 nm, as K_d for wavelengths longer than 550 nm for such oligotrophic waters mainly represents the absorption coefficient of pure seawater, which is considered as a global constant except for their slight variations with temperature and salinity [*Pegau et al*., 1997].

[32] $R_{rs}(\lambda)$ was computed from measurements of downwelling irradiance above the sea surface ($E_s(\lambda)$; $W/m^2/nm$) and water-leaving radiance ($L_w(\lambda)$, $W/m^2/nm/sr$), where the latter was computed from the measured nadir upwelling radiance ($L_u(\lambda)$; $W/m^2/nm/sr$) at a depth of 20 cm below the ocean surface. $L_u(\lambda)$ were then propagated to the sea surface using an iterative approach [*Mueller et al*., 2003] that estimates the spectral diffuse attenuation coefficient from spectral ratios of measured radiance, and $L_w(\lambda)$ is then computed based on Fresnel reflectance and the real relative index of refraction of seawater [*Mueller et al*., 2003]. Measurement of both $E_s(\lambda)$ and $L_u(\lambda)$ was made using a modified hyperspectral profiling radiometer (HyperPro, Satlantic, Inc.) adapted to float at the sea surface and tethered such that the instrument operated at a distance of ~100 m from the vessel. Instrument tilt was measured directly, and measurements were rejected if tilts exceeded 5°. Radiometric observations were subject to the same calibration, characterization, and quality control as for the profiling sensors.

5. Results and Discussion

5.1. Metrics to Evaluate Algorithm Performance

[33] Several measures were used to evaluate the K_d algorithm performance. First, a percentage difference (PD) between the profile-K_d and IOPs-K_d was calculated as

$$\mathrm{PD} = \frac{Q^{ret} - Q^{mer}}{Q^{mer}}. \tag{16}$$

[34] Here, Q^{mer} represents K_d derived from the E_d profiles, while Q^{ret} represents K_d retrieved from the spectral

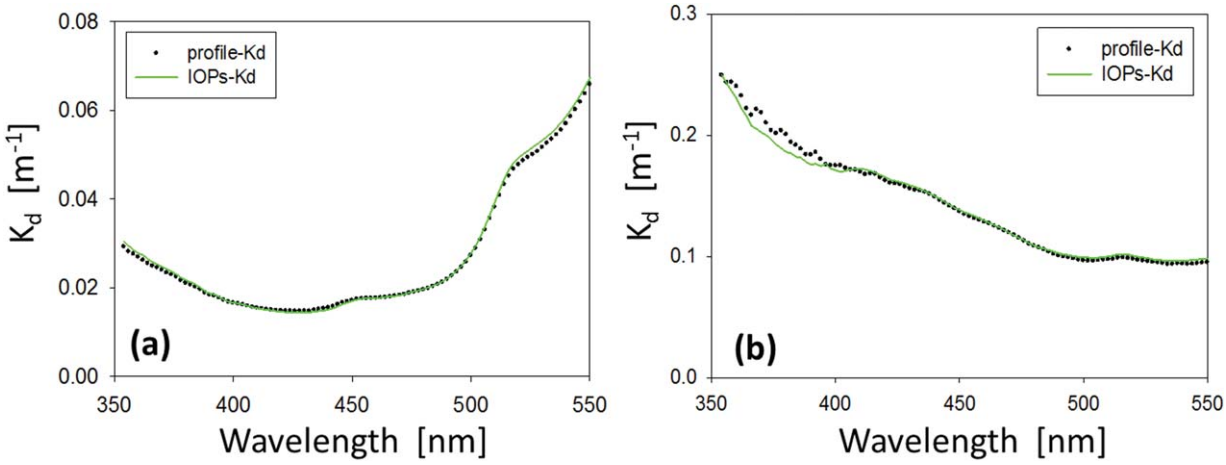

Figure 2. Examples showing remotely sensed $K_d(\lambda)$ compared with profile $K_d(\lambda)$ for (a) clear water (South Pacific Gyre) and (b) turbid water (Coast of Chile).

R_{rs}. Averaged signed percentage difference (ASPD) was further calculated as the arithmetic average of PD from all data points for a given wavelength, which provides a measure of systematic bias [*Zibordi et al.*, 2009]. Averaged absolute percentage difference (AAPD) was also calculated as the arithmetic average of absolute PD from all data points, which provides a measure of the overall closure between the two data sets.

[35] In addition, a root-mean-square difference (calculated in log-transformed data in order to cover a large dynamic range) was used to gauge the relative difference between the two data sets:

$$\mathrm{RMSD} = \sqrt{\frac{1}{N}\sum \left(\log_{10}(Q^{mer}) - \log_{10}(Q^{ret})\right)^2}. \qquad (17)$$

5.2. Evaluation of the IOPs-K_d Algorithm Performance

[36] As an example, Figure 2 compares IOPs-$K_d(\lambda)$ against profile-$K_d(\lambda)$ for two representative scenarios: clear water (Figure 2a; South Pacific Gyre) and relatively turbid water (Figure 2b; Coast of Chile) from the BIOSOPE data set. The two independently determined $K_d(\lambda)$ match each other very well in both magnitude and spectral shape (spectrally averaged AAPD is ~3% for both stations). Note that here the measured R_{rs} is hyperspectral, thus the correction of Raman effect is also hyperspectral. For this correction, *RF* values at the MODIS bands (412–667 nm) were first calculated for a given remote-sensing measurement as described in section 3.2. This multiband *RF* was then interpolated and extrapolated to obtain a hyperspectral *RF* (350–550 nm, every 2 nm) to match the spectral range and resolution of the measured data. Further, all *RF* values for wavelengths shorter than 400 nm were set to 0 to represent the assumed low Raman-scattering contribution in these bands.

[37] The spectral variations of ASPD and AAPD, between the IOPs-K_d and the profile-K_d of the BIOSOPE data set, are presented in Figure 3. ASPD of the IOPs-K_d oscillates around 0 (±5%), indicating negligible or no systematic bias in the IOPs-K_d. AAPD shows a range of ~7–15% for wavelengths between 350 and 550 nm. While AAPD is relatively high (~15%) around 420 nm for unknown reasons, the corresponding ASPD is only ~3%, suggesting that the relatively large differences are rather random. Linear regression analysis (see Figure 4) yielded a coefficient of determination (R^2) of 0.94, with a slope of 0.85 and an intercept of ~0.005 m^{-1}. The lower slope is mainly due to an underestimation of K_d in one of the three relatively turbid stations. For the oligotrophic waters ($K_d < 0.12$ m^{-1}), the slope is 0.93 and the bias is ~0.002 m^{-1}. These results indicate overall consistency between the IOPs-K_d (retrieved) and the profile-K_d (measured). This is especially promising considering that the processing and model coefficients used in the IOPs-K_d are completely independent of the profile-K_d, where there are various measurement and processing uncertainties as well as approximations in both IOPs-K_d and profile-K_d.

[38] Additional evaluation was performed by comparing IOPs-K_d with K_d derived from other established and easily applicable models. For the BIOSOPE data set, K_d values in

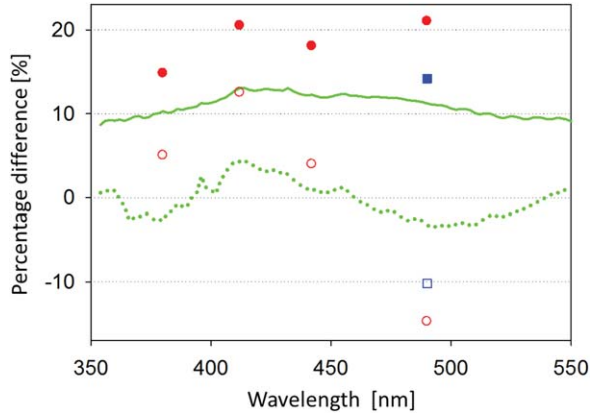

Figure 3. Spectrum of relative difference between remotely sensed $K_d(\lambda)$ and measured $K_d(\lambda)$. Solid curve: AAPD of the IOPs-K_d; dashed curve: ASPD of the IOPs-K_d. Solid symbols: AAPD of PCA-K_d (circle) and ratio-K_d (square). Open symbols: ASPD of PCA-K_d (circle) and ratio-K_d (square).

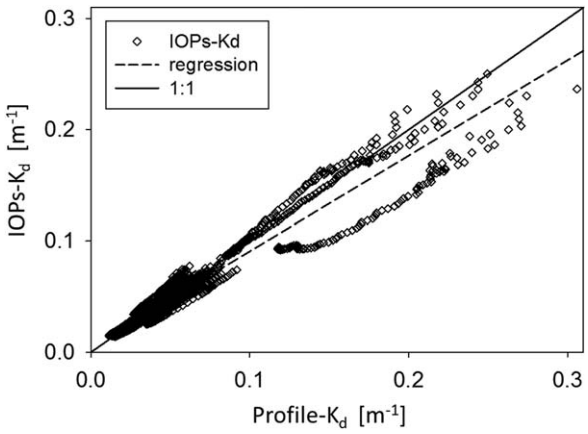

Figure 4. Scatter plot showing IOPs-K_d compared with profile-K_d for the BIOSOPE data set for 350–550 nm.

discrete short wavelengths (380, 412, 442, and 490 nm) by the Principle Component Analysis (PCA) of R_{rs} [*Fichot et al*., 2008] as well as K_d(490) by the operational band ratio of R_{rs} (http://oceancolor.gsfc.nasa.gov/cgi/algorithms.cgi?a=10) were also generated and compared with profile-K_d, with results also shown in Figure 3. K_d(490) from both PCA and the ratio algorithms were found to systematically underestimate the profile-K_d(490) (ASPD $\sim -12\%$), possibly because the data set used for the algorithm developments (at least the PCA algorithm) has an insufficient representation of such hyperclear waters. Other than 490 nm, the PCA-K_d shows higher AAPD and ASPD values for 380, 412, and 442 nm. These higher AAPD or ASPD in the PCA and ratio derived K_d product could be due to the fact that these algorithms do not explicitly take account of variations in sun angle and the backscattering coefficient, where K_d in principle varies with both [*Gordon*, 1989; *Lee et al*., 2005b].

[39] To highlight the performance of the commonly used K_d(490), Figure 5a shows how IOPs-derived, PCA-derived, and ratio-derived K_d(490) compare with profile-K_d(490) for this BIOSOPE data set ($N = 24$), where the AAPD values are 11.2, 21.0, and 14.2% for the three methods, respectively. Further, Figure 5b compares the IOPs-K_d(490) with profile-K_d(490) for the NOMAD set, while results of statistical evaluation of the K_d products from the three algorithms are presented in Table 3. The IOPs-K_d(490) has nearly identical results compared to the ratio-derived K_d(490) for either the entire data set or a subset for clear waters, although the algorithm coefficients used in the IOPs-K_d approach are independent of the NOMAD $R_{rs} - K_d$ data set (the coefficients used in the ratio-K_d(490) algorithm were derived from an earlier version of the NOMAD R_{rs}-K_d data set). The PCA-K_d has slightly higher AAPD and RMSD values, mostly due to the underestimation for higher K_d(490) values ($K_d(490) > 0.5$ m^{-1}; not shown). Note that in these comparisons all stations were assumed to be cloud free as detailed information regarding the cloudiness of each measurement was not available. Separately, a few stations (two or three, depending on the wavelength) with profile-$K_d \leq 0.01$ m^{-1} were not included,

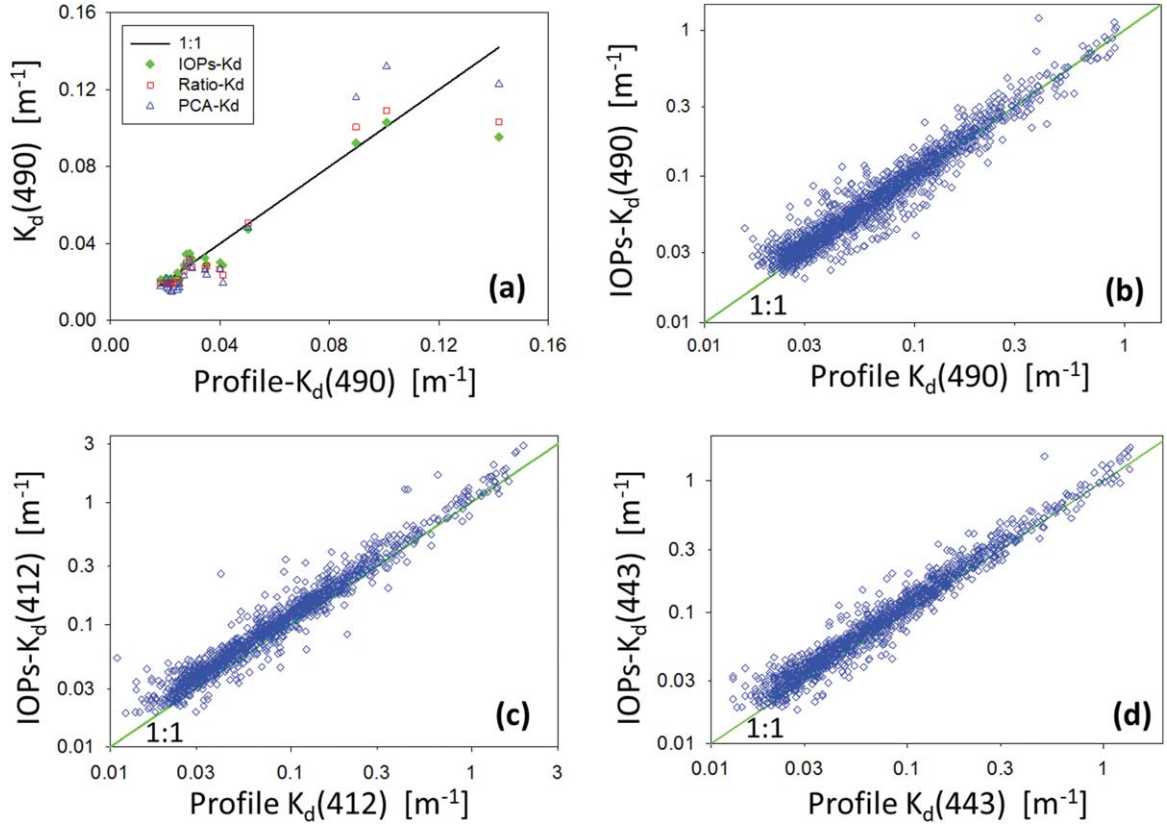

Figure 5. Comparison between retrieved K_d and profile-K_d. (a) The BIOSOPE data set, and at 490 nm. (b–d) The NOMAD data set, but limited to the IOPs results for clarity.

Table 3. Evaluation Results of the Three K_d Estimation Approaches When Applied to the NOMAD Set[a]

	All Data		For $K_d(490) \leq 0.2$ m−1	
	Linear Scale AAPD; R^2	Log10 Scale RMSD; R^2	Linear Scale AAPD; R^2	Log10 Scale RMSD; R^2
412 nm	($N = 1494$)		($N = 1387$)	
IOPs-K_d(412)	26.4%; 0.94	0.121; 0.95	24.7%; 0.87	0.112; 0.94
PCA-K_d(412)	24.8%, 0.94	0.148; 0.90	22.6%; 0.87	0.138; 0.87
443 nm	($N = 1516$)		($N = 1397$)	
IOPs-K_d(443)	20.7%; 0.97	0.103; 0.96	21.1%; 0.93	0.100; 0.94
PCA-K_d(443)	22.9%; 0.94	0.158; 0.92	23.3%; 0.88	0.147; 0.88
490 nm	($N = 1711$)		($N = 1570$)	
IOPs-K_d(490)	16.1%; 0.94	0.089; 0.94	16.6%; 0.89	0.089; 0.90
Ratio-K_d(490)	15.3%; 0.88	0.093; 0.92	15.2%; 0.85	0.089; 0.89
PCA-K_d(490)	27.4%; 0.90	0.183; 0.88	29.7%; 0.85	0.188; 0.83
510 nm	($N = 1523$)		($N = 1414$)	
IOPs-K_d(510)	12.3%; 0.95	0.075; 0.92	12.5%; 0.87	0.077; 0.84

[a]Note that IOPs-K_d refers to the updated model developed in this study; and not all wavelengths have equal number of data points, and not all algorithms can produce K_d for each wavelength.

as this value is considered to be a theoretical minimum for natural waters [*Morel et al*., 2007b].

[40] Also included in Table 3 is the evaluation of K_d at 412, 443, and 510 nm that could be generated by the IOPs or the PCA approaches, with a visual comparison between IOPs-K_d and profile-K_d of the 412 and 443 nm included in Figure 5. The performances of the IOPs-K_d and PCA-K_d approaches are very similar for these two spectral bands. Compared to the performance at 490 nm, statistically larger differences (either the entire data set or the clearer water subset, see Table 3) between IOPs-K_d and profile-K_d were found for both K_d(412) and K_d(443), while smallest differences were found between IOPs-K_d and profile-K_d at 510 nm (PCA has no output at this wavelength). The relatively larger differences (∼22% in linear scale and ∼0.11 in RMSD) for both K_d(412) and K_d(443) of clearer waters are puzzling because the quality of field-measured $R_{rs}(\lambda)$ and $E_d(\lambda, z)$ should be higher. In addition to modeling limitations, an in-depth analysis of all the data characteristics including processing methods and cloudiness is required to pinpoint and understand the likely primary sources of these uncertainties. Nevertheless, differences of ∼22% in linear scale and ∼0.11 in RMSD suggest that the IOPs-K_d approach is very promising, because these uncertainties are much lower than those from the band-ratio chlorophyll algorithms [*O'Reilly et al*., 1998]. In particular, the algorithm coefficients in the band-ratio chlorophyll algorithms were tuned from the actual data, while the coefficients used in the IOPs-K_d approach were independent of the data set.

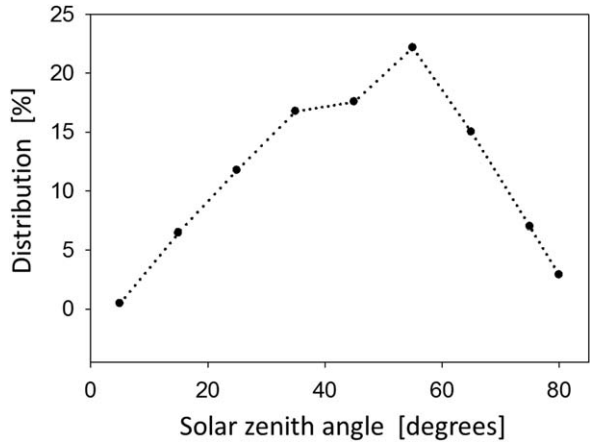

Figure 6. Percentage distribution of solar zenith angles in the NOMAD set related to K_d measurement.

[41] Note that the ratio-K_d and PCA-K_d approaches ignore the solar-angle variations in the algorithm development. As a large percentage (∼70%) of the NOMAD set has Sun angles in the 40°–70° range (see Figure 6), the ratio-K_d(490) derived from R_{rs} will thus be biased for large Sun angles. This systematic bias can be further manifested by partitioning the NOMAD data set into three subgroups based on sun angles: <30°, 30°–60°, and >60°. Figure 7 compares the retrieved K_d(490) from both models (ratio-K_d and IOPs-K_d) with profile-K_d(490) for $K_d(490) < 0.2$ m^{-1} (a total of 1570 data points, >92% of NOMAD), where the results of linear regression analysis are presented in Table 4. The choice of restricting K_d(490) to <0.2 m^{-1} was made for two reasons: (1) waters with $K_d(490) < 0.2$ m^{-1} are relatively clear where measured and retrieved K_d are more reliable than for other waters [*Mueller and Trees*, 1997]; (2) more than 98% of global waters have $K_d(490) < 0.2$ m^{-1}. When comparing the two retrieved K_d(490) with profile-K_d(490), the intercepts are nearly negligible (see Table 4), but the regression slopes show clear difference between the two algorithm approaches. The slopes of the ratio-K_d(490) show a clear relationship with sun angle: larger (1.07 slope) for low zenith angles (<30°), while smaller (0.92) for high zenith angles (>60°). This is consistent with radiative transfer calculations and the nature of the data set: K_d increases with sun angle (due primarily to the increased photon pathlength in water), while the data set has a high representation of sun angle in the 40°–70° range (see Figure 6). The IOPs-K_d, on the other hand, shows nearly identical slopes (close to unity) for the three subgroups, indicating that this explicit inclusion of sun angle in the model can very well take into account the influence of sun angle on the K_d variation, which can be as

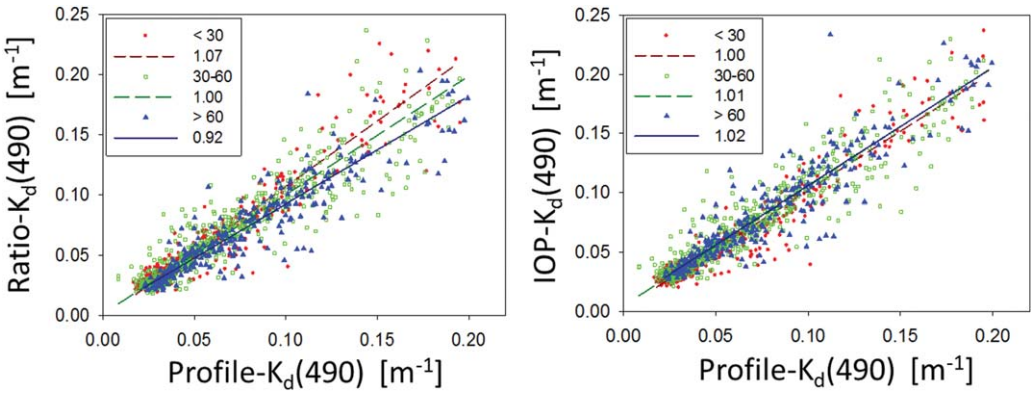

Figure 7. Comparison between retrieved $K_d(490)$ and profile-$K_d(490)$ for various sun angle ranges of the NOMAD data set for $K_d(490) < 0.2$ m^{-1}: (a) ratio-derived $K_d(490)$ and (b) IOPs-$K_d(490)$. The various regression lines are color coded and annotated with the regression slope values in the legend.

large as ~30% between Sun at zenith and Sun at 60° from zenith [*Gordon*, 1989; *Morel et al*., 2002]. Therefore, with the Sun angle variation explicitly taken into account in the IOPs-K_d model, not only uncertainties of estimated K_d are reduced but also a clear description regarding the AOP nature of K_d is also manifested.

[42] Further, because of this sun-angle dependent nature of K_d and the diurnal variation of solar elevation, K_d is also a diurnal (time dependent) property. Therefore, there is a necessity to redefine or modify the short-term (daily, 8 day composite, and monthly composite) K_d products from satellite ocean color missions. This is because, even for stable optical properties in daily or monthly temporal scales, the present, ratio-derived, $K_d(490)$ of a location from daily satellite overpass to the best represents a diffuse attenuation coefficient with a Sun angle of ~45°. This angle-fixed $K_d(490)$ product does not represent the diffuse attenuation coefficient of the daily solar radiation. Because of this mismatch in solar angles, large errors could be resulted in the estimated daily $E_d(z, \lambda)$ if a combination of daily $E_d(0, \lambda)$ and the instantaneous $K_d(\lambda)$ is used. However, with the sun-angle explicit IOPs-K_d model, the impact on this mismatch on $E_d(z, \lambda)$ estimation can be corrected (J. Wei et al, Model of the Attenuation Coefficient of Daily Photosynthetically Available Radiation in the Upper Ocean, submitted to Method in Oceanography, 2013). Furthermore, the inclusion of sun angle in the semianalytical model enables diurnal calculation of photoacclamation light at the bottom of the mixed layer [*Behrenfeld et al*., 2006; *Letelier et al*., 2004].

[43] It is necessary to point out that in the R_{rs}-IOPs inversion and the IOPs-K_d retrievals, the backscattering coefficients of pure seawater (b_{bw}) reported in *Zhang and Hu* [2009] were used. Their values are ~18% lower than those in *Morel* [1974]. If the b_{bw} values of *Morel* [1974] are used instead, 4–8% higher K_d will be obtained for the short wavelengths (350–400 nm), and such percentage differences increase with decreasing wavelengths. The impact is negligible for less clearer waters, however.

6. Implications for Ocean Physics and Biogeochemistry Studies

6.1. Penetration of UV Radiation

[44] The availability of UV radiation at different depths is important to many photochemical and biological processes [*Arrigo and Brown*, 1996; *Cullen et al*., 2012; *Cullen and Neale*, 1994; *Gao et al*., 2012; *Hader et al*., 2007; *Tedetti and Sempere*, 2006; *Zepp et al*., 2006]. Numerous studies have been carried out in the past decades to document the penetration of UV radiation in the global oceans [*Ahmad et al*., 2003; *Conde et al*., 2000; *Johannessen et al*., 2003; *Lehmann et al*., 2004; *Smyth*, 2011; *Vasilkov et al*., 2001], and most of the remote-sensing evaluations were based on the Case-1 assumptions [*Morel and Maritorena*, 2001], i.e., optical properties of the bulk water can be quantified based on Chl. However, results from field measurements have indicated that the absorption coefficient in the UV domain could not be described accurately using Chl [*Morel et al*., 2007a; *Vasilkov et al*., 2002].

[45] To obtain an IOPs-based evaluation and understanding of solar propagation in the shorter wavelengths, we here calculated the penetration of 360 nm within the UVA spectral range. To quantify the penetration of this light, the

Table 4. Results of Linear Regression Between Profile and Retrieved $K_d(490)$ for Three Subgroups of the NOMAD Set With Different Sun Angles and for $K_d(490) \leq 0.2$ m^{-1}[a]

	Ratio-$K_d(490)$			IOPs-$K_d(490)$		
Range of Sun Zenith Angle	Slope	Intercept (m^{-1})	R^2	Slope	Intercept (m^{-1})	R^2
<30° (408)	1.07	−0.002	0.92	1.00	0.001	0.93
30°–60° (909)	1.02	0.000	0.82	1.01	0.004	0.89
>60° (253)	0.92	0.002	0.81	1.02	0.004	0.84

[a]Numbers in the parenthesis after the sun angle represent numbers of data points, and the total number of data points is 1570 (92% of NOMAD). Note that IOPs-K_d refers to the updated model developed in this study.

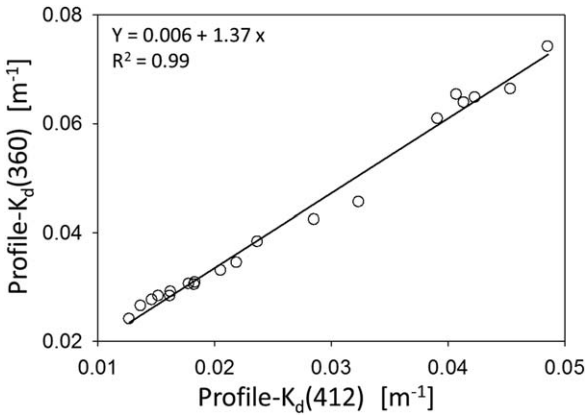

Figure 8. Relationship between measured $K_d(412)$ and $K_d(360)$ from the BIOSOPE data set ($N = 20$).

depth ($Z(360)_{10\%}$) corresponding to 10% of its surface value [*Ahmad et al*., 2003; *Vasilkov et al*., 2001] is calculated from $K_d(360)$,

$$Z(360)_{10\%} = \frac{2.3}{K_d(360)}, \tag{18}$$

and the distribution of $Z(360)_{10\%}$ in the global oceans is further calculated from annual composite of MODIS data. Note that the MODIS composite represents an annual mean of R_{rs}. Because of the nonlinear relationship between R_{rs} and IOPs and the angular mismatch between the instantaneous $K_d(360)$ (calculated with the Sun at zenith) and the diffuse attenuation coefficient representing the annual irradiance (see discussion in section 5 regarding effect of solar elevation), the calculated $Z(360)_{10\%}$ from this annual composite does not exactly equal the true annual mean penetration of this irradiance. High-temporal resolution (3 h or finer) products [*Vasilkov et al*., 2001] should be calculated first in order to compose such an annual mean. However, this $Z(360)_{10\%}$ from annual R_{rs} is sufficient to provide a general picture of its dynamic range and its spatial variability around local noon.

[46] Historically, many studies used either CDOM absorption or DOC concentrations to empirically estimate K_d in the UV [*Huovinen et al*., 2003; *Williamson et al*., 1996]. These approaches generally take into account the contributions of the absorption coefficient to K_d, but ignore the contribution of backscattering [*Gordon*, 1989]. On the other hand, the backscattering coefficient for pure water could contribute 50% or more to K_d in the short wavelengths for clear waters.

[47] To estimate $K_d(360)$ analytically, as shown above, it requires $a(360)$ and $b_b(360)$, which can be derived from the R_{rs}-IOPs inversion, where R_{rs}(360-visible) is either measured in the field or derived from satellite measurements. Unfortunately, past and current ocean color sensors do not have UV bands for the direct IOPs and K_d retrievals at 360 nm. To circumvent this difficulty before a future satellite ocean color sensor with UV bands is available (e.g., NASA's Pre-Aerosol, Clouds, and ocean Ecosystem (PACE) mission, http://decadal.gsfc.nasa.gov/pace.html), similarly as in *Hojerslev and Aas* [1991], we used the "shortest" MODIS wavelength, 412 nm, for the estimation of $K_d(360)$. This is because the spectral dependences of IOPs are not stable, and the longer the wavelength gap, the lower the accuracy in K_d extrapolations. Here, $K_d(412)$ is first estimated using the IOPs-K_d approach, and $K_d(360)$ is then calculated as

$$K_d(360) = 0.006 + 1.37K_d(412). \tag{19}$$

[48] This relationship ($R^2 = 0.99$, $N = 20$, see Figure 8) is developed from the in situ BIOSOPE measurements and limited to the clear-water stations ($K_d(412) \le 0.05$ m^{-1}). Different empirical coefficients would be derived if a wider $K_d(412)$ range were to be used. The choice of $K_d(412) \le 0.05$ m^{-1} was for two reasons. First, most of the BIOSOPE data set covers $K_d(412) \le 0.05$ m^{-1}. The remaining four measurements with $K_d(412) > 0.05$ m^{-1} may not be representative enough to obtain a solid relationship between $K_d(412)$ and $K_d(360)$. Second, >50% of the global oceans show $K_d(412) < 0.05$ m^{-1} according to MODIS observations.

[49] To derive $Z(360)_{10\%}$ distributions in the global oceans, a MODIS annual composite of $R_{rs}(\lambda)$ for 2004, as an example, was obtained from NASA Goddard Space Flight Center, and was used to derive $a(412)$ and $b_b(412)$ following the R_{rs}-IOPs inversion approach articulated in section 3. Then, global $K_d(412)$ with a zenith Sun was derived using the IOPs-K_d model (equation 5 and Table 1, with $\theta_s = 0°$), which was further used to derive $K_d(360)$ (also Sun at zenith) using the in situ-based empirical relationship (equation 19). Finally, $Z(360)_{10\%}$ of noon time was derived from $K_d(360)$ using equation (18). The derived global distribution of noontime $Z(360)_{10\%}$ is presented in Figure 9, where locations with $K_d(412) > 0.05$ m^{-1} are masked out (white color). For the oligotrophic oceans, $Z(360)_{10\%}$ is generally around 60 m, and can be as deep as 70–80 m for gyre waters. These values are in general consistent with the observations of *Vasilkov et al*. [2001] and *Smyth* [2011]. This means that on an annual average and when the Sun is at zenith, significant UVA light is present within or even below the surface mixed layer [*Ahmad et al*., 2003], as this depth could be within 50 m for a large portion of the global oceans (http://www.nodc.noaa.gov/OC5/WOA94/mix.html) [*Monterey and Levitus*, 1997]. Since UV radiation could either enhance or prohibit phytoplankton photosynthesis [*Gao et al*., 2012; *Smith and Cullen*, 1995; *Tedetti and Sempere*, 2006], it is important to know the UV radiation availability in the water column and their spatial and temporal distributions in the global oceans [*Ahmad et al*., 2003; *Cullen and Neale*, 1994; *Vasilkov et al*., 2001].

6.2. PhotoActive Depth

[50] Historically, the euphotic zone depth (Z_{eu}) is used to represent the layer of water where net photosynthesis is positive. As a rule of thumb, Z_{eu} is practically defined as the depth where the spectrally integrated radiation in the 400–700 nm range (photosynthetically active radiation (PAR)) is 1% of its surface value [*Ryther*, 1956]. In the primary production models, Z_{eu} is commonly used as a scaling factor in order to get the integrated primary production of the water column [*Arrigo et al*., 1998; *Behrenfeld and Falkowski*, 1997]. However, it is well known that for the 400–700 nm spectral range the red photons (600–700 nm) quickly disappear in the upper few meters, and it is the blue-green photons that penetrate to the deeper ocean

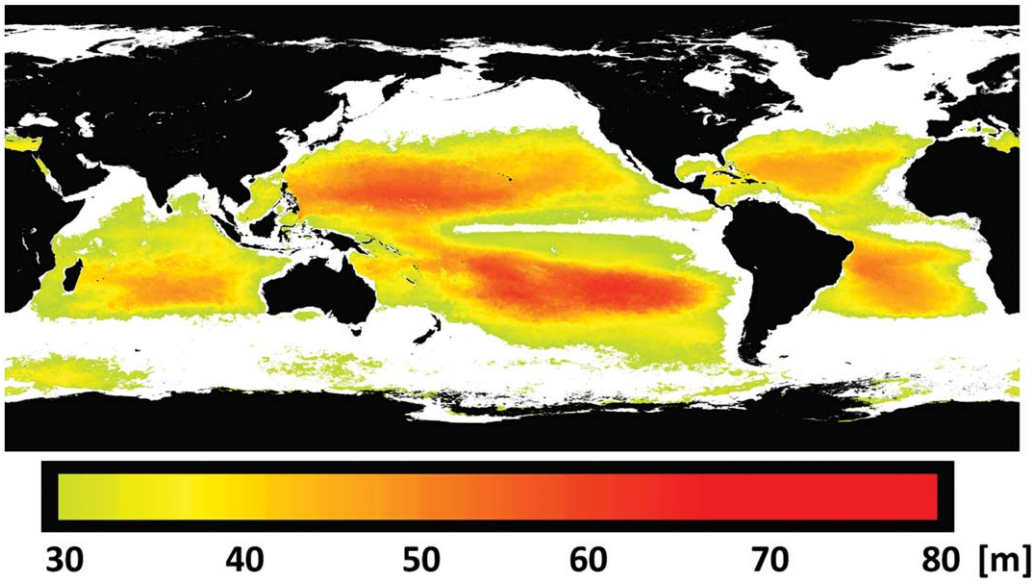

Figure 9. Penetration depth of solar irradiance (sun at zenith) at 360 nm in the global oceans, as gauged by 10% of the surface light ($Z(360)_{10\%}$). Black: land or ice; white: waters with $K_d(412) > 0.05$ m^{-1} and are masked out here.

[*Morel and Antoine*, 1994; *Paulson and Simpson*, 1977]. Further, phytoplankton absorb most efficiently in the blue to blue-green portion of the spectrum [*Bricaud et al*., 1995; *Sathyendranath et al*., 1987], and together with UV radiation, it is the spectral region most important for photoactive processes (e.g., photo-oxidation of color dissolved organic matter (CDOM) [*Moran and Zepp*, 1997, and references therein]). It is thus interesting to know the difference between the penetration depth of the blue-green light (Z_{bg}) [*Gnanadesikan and Anderson*, 2009; *Manizza et al*., 2005] and the penetration depth of PAR (Z_{eu}).

[51] For this comparison, we also started from the MODIS annual composite R_{rs} data in 2004. The IOPs (a and b_b) of the first four MODIS bands (412, 443, 488, and 531 nm) were then derived following the R_{rs}-IOPs inversion procedures described in section 3. Z_{eu} was calculated using $a(488)$ and $b_b(488)$ as described in *Lee et al*. [2007], which has been validated for various locations of marine waters [*Lee et al*., 2007; *Shang et al*., 2010; *Zhao et al*., 2013]. Z_{bg} is defined as the arithmetic average of the 1% depth of the four blue-green bands. For instance, for 412 nm, its 1% depth is $Z(412)_{1\%} = 4.6/K_d(412)$. Again, all of these calculations assumed a solar zenith angle of 0°, i.e., the Sun is at zenith and cloud free. As discussed in section 5, because of the diurnal variation in solar elevation, these light depths will be deeper than the actual annual mean depth of either PAR or the blue-green bands. Their relative difference, however, is informative if the two penetration depths are similar in the global oceans.

[52] The percentage difference between Z_{bg} and Z_{eu} was calculated as

$$PD_z = \frac{Z_{bg} - Z_{eu}}{Z_{eu}}. \quad (20)$$

[53] Figure 10 shows the global distributions of PD_z. For oceanic waters, Z_{bg} is generally 30–40% deeper than Z_{eu}. For instance, for the south Pacific gyre, Z_{eu} is about 140 m [also see *Morel et al*., 2007a] while Z_{bg} is approaching 190 m, which can be well below the mixed layer depth [*Monterey and Levitus*, 1997]. This indicates that for such ocean layers where there are adequate nutrients, there is also adequate, high-quality (suitable for photosynthesis) light available at least during noon time. This is consistent with observations by *Morel and Berthon* [1989] and *Letelier et al*. [2004], where the depth of the deep chlorophyll maxima (DCM) is generally deeper than Z_{eu} for oceanic waters. Indeed, at the depth of Z_{eu}, there is still ~3–4% of surface blue-green light available. Because the blue-green spectral range contributes the most to phytoplankton photosynthesis, the availability of the blue-green light could help explain the location of the DCM in oceanic waters.

[54] In contrast to most oceanic waters where Z_{bg} is deeper than Z_{eu}, some coastal waters and inland lakes show the opposite trend, i.e., Z_{bg} is about 20–30% shallower than Z_{eu}, for example in coastal waters of the northern Gulf of Mexico and Lake Erie. Z_{bg} of the Yellow Sea is also found to be shallower (~10–20%) than Z_{eu}. This suggests that in these regions the absorption coefficients in the blue-green bands are comparable to or higher than the average absorption between 400 and 700 nm, resulting in a photoactive depth (Z_{bg}) shallower than the euphotic-zone depth. Clearly, depending on the research objectives, different light availability depths may be required and used.

7. Summary and Conclusions

[55] Understanding photoactive processes in the ocean such as primary production and CDOM oxidation requires accurate knowledge on the availability of the spectral light instead of the integrated light, where the former is governed by the spectral diffuse attenuation coefficient ($K_d(\lambda)$). For the estimation of $K_d(\lambda)$ from remote sensing measurements, the previously developed semianalytical

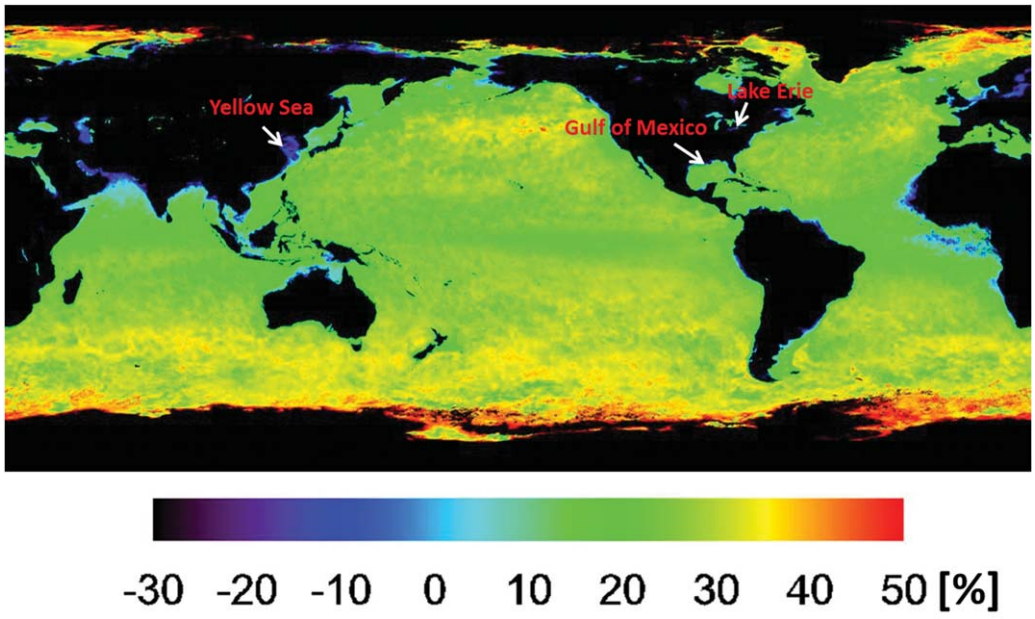

Figure 10. Percentage difference between the 1% penetration depth (the Sun at zenith) of the blue-green light (Z_{bg}) and the euphotic-zone depth (Z_{eu}).

approach centered on the water's IOPs is revised here based on radiative transfer and Hydrolight simulations. The updated model not only explicitly takes into account the contributions of absorption and backscattering coefficients and the impact of sun angle, but also includes the effects of phase function shifts between molecular and particulate scattering. In addition, a simple empirical procedure is developed here to correct the Raman effect when processing ocean-color satellite data over oceanic waters.

[56] Through validations using independent data sets collected from the superclear waters of the south Pacific as well as compiled over various regions of the global oceans, the IOPs-based approach has been shown to be effective in retrieving K_d from the UVA to the visible with acceptable uncertainties. In particular, because of the explicit inclusion of sun angle in the IOPs-K_d model, the approach also provides unequivocal meaning of the K_d product as an AOP and its instantaneous nature. This relationship further paves an easy route for the generation of diurnal-averaged K_d or penetration depth of the global oceans from satellite ocean color measurements. Such products will be more applicable for the studies of ocean physics and ocean biogeochemistry as instantaneous K_d or instantaneous penetration depth do not represent the attenuation of solar irradiance during a day even for stable water and air properties.

[57] Further, the IOPs-K_d approach is applicable to all wavelengths where satellite measurements are available, including the UV bands on future satellite missions. The produced MODIS sample global products with the Sun at zenith showed that the actual penetration depth of the blue-green light is ~30–40% deeper than the commonly used euphotic zone depth in oceanic waters. This feature helps explain previously reported deep chlorophyll maximum in oceanic waters. In addition, MODIS data also show that at a depth of 50–70 m in oceanic waters there is still ~10% of the surface UVA (at 360 nm) radiation when the Sun is at zenith.

[58] Although the data used in this study for the K_d validation, especially for clear waters, are limited, the in situ-based validation results and MODIS-based products both suggest that generation of spectrally explicit estimates of K_d or penetration depths from satellite ocean color missions would help develop and improve understanding of biological and biogeochemical processes at depth. In addition, for accurate application of daily surface irradiance products in studying water column heat transfer and phytoplankton photosynthesis, data products of diurnal-averaged K_d or penetration depth should be produced from satellite ocean color missions.

[59] **Acknowledgments.** We are grateful to the financial support from the NASA Ocean Biology and Biogeochemistry and Water and Energy Cycle Programs (Lee, Hu) and the JPSS VIIRS Ocean Color Cal/Val Project (Arnone, Lee), from the National Natural Science Foundation of China (41071223, Du; 40976068 and 41121091, Shang) and the Ministry of Science and Technology of China (2013BAB04B00, Shang). The acquisition of BIOSOPE data where funded through CNRS(1)-INSU(2) grants. We are in debt to Jeremy Werdell and data collectors shared their valuable data with the community through the NASA SeaBASS, and we thank the NASA OBPG for providing MODIS ocean-color products. Fang Gao of the Department of Marine Science at the University of Georgia helped to implement the PCA-K_d routine. We thank the three anonymous reviewers for their helpful comments and suggestions.

References

Åas, E. (1987), Two stream irradiance model for deep waters, *Appl. Opt.*, *26*, 2095–2101.

Ahmad, Z., J. R. Hermanb, A. Vasilkovc, M. Tzortzioud, G. Mitchell, and M. Kahru (2003), Seasonal variation of UV radiation in the ocean under clear and cloudy conditions, paper presented at Ultraviolet Ground- and Space-based Measurements, Models, and Effects III, SPIE, Bellingham, Wash.

Arrigo, K., D. Worthen, A. Schnell, and M. P. Lizotte (1998), Primary production in Southern Ocean waters, *J. Geophys. Res.*, *103*, 15587–15600, doi:10.1029/98JC00930.

Arrigo, K. R., and C. W. Brown (1996), Impact of chromophoric dissolved organic matter on UV inhibition of primary productivity in the sea, *Mar. Ecol. Prog. Ser.*, *140*, 207–216.

Austin, R. W., and T. J. Petzold (1981), The determination of the diffuse attenuation coefficient of sea water using the coastal zone color scanner, in *Oceanography from Space*, edited by J. F. R. Gower, pp. 239–256, Plenum, New York.

Austin, R. W., and T. J. Petzold (1986), Spectral dependence of the diffuse attenuation coefficient of light in ocean waters, *Opt. Eng.*, *25*, 473–479.

Bartlett, J. S., K. J. Voss, S. Sathyendranath, and A. Vodacek (1998), Raman Scattering by pure water and seawater, *Appl. Opt.*, *37*, 3324–3332.

Behrenfeld, M. J., and P. G. Falkowski (1997), Photosynthetic rates derived from satellite-based chlorophyll concentration, *Limnol. Oceanogr.*, *42*, 1–20.

Behrenfeld, M. J. et al. (2006), Climate-driven trends in contemporary ocean productivity, *Nature*, *444*, 752–755, doi:10.1038/nature05317.

Berwald, J., D. Stramski, C. D. Mobley, and D. A. Kiefer (1995), Influences of absorption and scattering on vertical changes in the average cosine of the underwater light field, *Limnol. Oceanogr.*, *40*, 1347–1357.

Bricaud, A., M. Babin, A. Morel, and H. Claustre (1995), Variability in the chlorophyll-specific absorption coefficients of natural phytoplankton: Analysis and parameterization, *J. Geophys. Res.*, *100*, 13321–13332.

Conde, D., L. Aubriot, and R. Sommaruga (2000), Changes in UV penetration associated with marine intrusions and freshwater discharge in a shallow coastal lagoon of the Southern Atlantic Ocean, *Mar. Ecol. Prog. Ser.*, *207*, 19–31.

Cullen, J. J., and P. J. Neale (1994), Ultraviolet radiation, ozone depletion, and marine photosynthesis, *Photosyn. Res.*, *39*, 303–320.

Cullen, J. J., R. F. Davis, and Y. Huot (2012), Spectral model of depth-integrated water column photosynthesis and its inhibition by ultraviolet radiation, *Global Biogeochem. Cycles*, *26*, GB1011, doi:10.1029/2010GB003914.

Darecki, M., and D. Stramski (2004), An evaluation of MODIS and SeaWiFS bio-optical algorithms in the Baltic Sea, *Remote Sens. Environ.*, *89*, 326–350.

Del Vecchio, R., and N. V. Blough (2002), Photobleaching of chromophoric dissolved organic matter in natural waters: Kinetics and modeling, *Mar. Chem.*, *78*, 231–253.

Dunne, R. P., and B. E. Brown (1996), Penetration of solar UVB radiation in shallow tropical waters and its potential biological effects on coral reefs; Results from the central Indian Ocean and Andaman Sea, *Mar. Ecol. Prog. Ser.*, *144*, 109–118.

Fichot, C., S. Sathyendranath, and W. Miller (2008), SeaUV and SeaUVC: Algorithms for the retrieval of UV/Visible diffuse attenuation coefficients from ocean color, *Remote Sens. Environ.*, *112*, 1584–1602.

Gao, K., E. W. Helbling, D.-P. Häder, and D. A. Hutchins (2012), Responses of marine primary producers to interactions between ocean acidification, solar radiation, and warming, *Mar. Ecol. Prog. Ser.*, *470*, 167–189.

Gnanadesikan, A., and W. G. Anderson (2009), Ocean water clarity and the ocean general circulation in a coupled climate model, *J. Phys. Oceanogr.*, *39*, 314–332.

Gnanadesikan, A., K. Emanuel, G. A. Vecchi, W. G. Anderson, and R. Hallberg (2010), How ocean color can steer Pacific tropical cyclones, *Geophys. Res. Lett.*, *37*, L18802, doi:10.1029/2010GL044514.

Gordon, H. R. (1989), Can the Lambert-Beer law be applied to the diffuse attenuation coefficient of ocean water?, *Limnol. Oceanogr.*, *34*, 1389–1409.

Gordon, H. R., and D. K. Clark (1980), Remote sensing optical properties of a stratified ocean: An improved interpretation, *Appl. Opt.*, *19*, 3428–3430.

Gordon, H. R., and W. R. Mcluney (1975), Estimation of the depth of sunlight penetration in the sea for remote sensing, *Appl. Opt.*, *14*, 413–416.

Gordon, H. R., M. R. Lewis, S. D. McLean, M. S. Twardowski, S. A. Freeman, K. J. Voss, and G. C. Boynton (2009), Spectra of particulate backscattering in natural waters, *Opt. Express*, *17*, 16,192–16,208.

Gregg, W. W., and K. L. Carder (1990), A simple spectral solar irradiance model for cloudless maritime atmospheres, *Limnol. Oceanogr.*, *35*, 1657–1675.

Gueymard, C. A. (2001), Parameterized transmittance model for direct beam and circumsolar spectral irradiance, *Solar Energy*, *71*, 325–346.

Hader, D.-P., H. D. Kumar, R. C. Smith, and R. C. Worrest (2007), Effects of solar UV radiation on aquatic ecosystems and interactions with climate change, *Photochem. Photobiol. Sci.*, *6*, 267–285.

Hojerslev, N. K., and E. Aas (1991), A relationship for the penetration of ultraviolet-B radiation into the Norwegian Sea, *J. Geophys. Res.*, *96*, 17003–17005.

Hu, C., and K. J. Voss (1997), In situ measurements of Raman scattering in clear ocean water, *Appl. Opt.*, *36*, 6962–6967.

Hu, C., Z. Lee, and B. Franz (2012), Chlorophyll a algorithms for oligotrophic oceans: A novel approach based on three-band reflectance difference, *J. Geophys. Res.*, *117*, C01011, doi:10.1029/2011JC007395.

Huovinen, P. S., H. Penttila, and M. R. Soimasuo (2003), Spectral attenuation of solar ultraviolet radiation in humic lakes in Central Finland, *Chemosphere*, *51*, 205–214.

IOCCG (2006), Remote sensing of inherent optical properties: Fundamentals, tests of algorithms, and applications, *Rep. 5*, edited by Z.-P. Lee, p. 126, Int. Ocean-Colour Coord. Group, Dartmouth, N. S., Canada.

Jamet, C., H. Loisel, and D. Dessailly (2012), Retrieval of the spectral diffuse attenuation coefficient Kd(λ) in open and coastal ocean waters using a neural network inversion, *J. Geophys. Res.*, *117*, C10023, doi:10.1029/2012JC008076.

Johannessen, S. C., W. L. Miller, and J. J. Cullen (2003), Calculation of UV attenuation and colored dissolved organic matter absorption spectra from measurements of ocean color, *J. Geophys. Res.*, *108*(C9), 3301, doi:10.1029/2000JC000514.

Jolliff, J. K., T. A. Smith, C. N. Barron, S. deRada, S. C. Anderson, R. W. Gould, and R. A. Arnone (2012), The impact of coastal phytoplankton blooms on ocean-atmosphere thermal energy exchange: Evidence from a two-way coupled numerical modeling system, *Geophys. Res. Lett.*, *39*, L24607, doi:10.1029/2012GL053634.

Kieber, R. J., X. Zhou, and K. Mopper (1990), Formation of carbonyl compounds from UV-induced photodegradation of humic substances in natural waters: Fate of Riverine carbon in the sea, *Limnol. Oceanogr.*, *35*, 1503–1515.

Kirk, J. T. O. (1984), Dependence of relationship between inherent and apparent optical properties of water on solar altitude, *Limnol. Oceanogr.*, *29*, 350–356.

Kirk, J. T. O. (1988), Solar heating of water bodies as influenced by their inherent optical properties, *J. Geophys. Res.*, *93*, 10,897–10,908.

Lee, Z., K. Carder, S. Hawes, R. Steward, T. Peacock, and C. Davis (1994), Model for interpretation of hyperspectral remote-sensing reflectance, *Appl. Opt.*, *33*, 5721–5732.

Lee, Z. P., and C. Hu (2006), Global distribution of Case-1 waters: An analysis from SeaWiFS measurements, *Remote Sens. Environ.*, *101*, 270–276.

Lee, Z. P., K. L. Carder, and R. Arnone (2002), Deriving inherent optical properties from water color: A multi-band quasi-analytical algorithm for optically deep waters, *Appl. Opt.*, *41*, 5755–5772.

Lee, Z. P., K. L. Carder, and K. P. Du (2004), Effects of molecular and particle scatterings on model parameters for remote-sensing reflectance, *Appl. Opt.*, *43*, 4957–4964.

Lee, Z. P., M. Darecki, K. L. Carder, C. Davis, D. Stramski, and W. J. Rhea (2005a), Diffuse attenuation coefficient of downwelling irradiance: An evaluation of remote sensing methods, *J. Geophys. Res.*, *110*, C02017, doi:10.1029/2004JC002573.

Lee, Z. P., K. P. Du, and R. Arnone (2005b), A model for the diffuse attenuation coefficient of downwelling irradiance, *J. Geophys. Res.*, *110*, C02016, doi:10.1029/2004JC002275.

Lee, Z. P., A. Weidemann, J. Kindle, R. Arnone, K. L. Carder, and C. Davis (2007), Euphotic zone depth: Its derivation and implication to ocean-color remote sensing, *J. Geophys. Res.*, *112*, C03009, doi:10.1029/2006JC003802.

Lee, Z. P., S. Shang, C. Hu, M. Lewis, R. Arnone, Y. Li, and B. Lubac (2010), Time series of bio-optical properties in a subtropical gyre: Implications for the evaluation of inter-annual trends of biogeochemical properties, *J. Geophys. Res.*, *115*, C09012, doi:10.1029/2009JC005865.

Lee, Z. P., K. Du, K. J. Voss, G. Zibordi, B. Lubac, R. Arnone, and A. Weidemann (2011), An inherent-optical-property-centered approach to correct the angular effects in water-leaving radiance, *Appl. Opt.*, *50*, 3155–3167.

Lehmann, M. K., R. F. Davis, Y. Huot, and J. J. Cullen (2004), Spectrally weighted transparency in models of water-column photosynthesis and photoinhibition by ultraviolet radiation, *Mar. Ecol. Prog. Ser.*, *269*, 101–110.

Lesser, M. P., and J. H. Farrell (2004), Exposure to solar radiation increases damage to both host tissues and algal symbionts of corals during thermal stress, *Coral Reefs*, *23*, 367–377.

Letelier, R. M., D. M. Karl, M. R. Abbott, and R. R. Bidigare (2004), Light driven seasonal patterns of chlorophyll and nitrate in the lower euphotic zone of the North Pacific Subtropical Gyre, *Limnol. Oceanogr.*, *49*, 508–519.

Lewis, M. R., M. Carr, G. Feldman, W. Esaias, and C. McMclain (1990), Influence of penetrating solar radiation on the heat budget of the equatorial pacific ocean, *Nature*, *347*, 543–545.

Loisel, H., and D. Stramski (2000), Estimation of the inherent optical properties of natural waters from the irradiance attenuation coefficient and reflectance in the presence of Raman scattering, *Appl. Opt.*, *39*, 3001–3011.

Manizza, M., C. L. Quere, A. J. Watson, and E. T. Buitenhuis (2005), Bio-optical feedbacks among phytoplankton, upper ocean physics and sea ice in a global model, *Geophys. Res. Lett.*, *32*, L05603, doi:10.1029/2004GL020778.

Marshall, B. R., and R. C. Smith (1990), Raman scattering and in-water ocean properties, *Appl. Opt.*, *29*, 71–84.

Mitchell, B. G., and M. Kahru (1998), Algorithms for SeaWiFS standard products data set, *Rep. 39*, pp. 133–147, Calif. Coop. Oceanic Fish. Invest.

Mobley, C. D. (1994), *Light and Water: Radiative Transfer in Natural Waters*, Academic, New York.

Mobley, C. D. (1995), *Hydrolight 3.0 Users' Guide*, SRI Int., Menlo Park, Calif.

Monterey, G., and S. Levitus (1997), *Seasonal Variability of Mixed Layer Depth for the World Ocean*, 96 pp., Gov. Print. Off., Washington, D. C.

Moran, M. A., and R. G. Zepp (1997), Role of photoreactions in the formation of biologically labile compounds from dissolved organic matter, *Limnol. Oceanogr.*, *42*, 1307–1316.

Morel, A. (1974), *Optical properties of pure water and pure sea water, in Optical Aspects of Oceanography*, edited by N. G. Jerlov and E. S. Nielsen, pp. 1–24, Academic, New York.

Morel, A. (1991), Light and marine photosynthesis: A spectral model with geochemical and climatological implications, *Prog. Oceanogr.*, *26*, 263–306.

Morel, A., and D. Antoine (1994), Heating rate within the upper ocean in relation to its bio-optical state, *J. Phys. Oceanogr.*, *24*, 1652–1665.

Morel, A., and J. F. Berthon (1989), Surface pigments, algal biomass profiles, and potential production of the euphotic layer: Relationships reinvestigated in review of remote-sensing applications, *Limnol. Oceanogr.*, *34*, 1545–1562.

Morel, A., and B. Gentili (1991), Diffuse reflectance of oceanic waters: Its dependence on sun angle as influenced by the molecular scattering contribution, *Appl. Opt.*, *30*, 4427–4438.

Morel, A., and B. Gentili (2004), Radiation transport within oceanic (case 1) water, *J. Geophys. Res.*, *109*, C06008, doi:10.1029/2003JC002259.

Morel, A., and S. Maritorena (2001), Bio-optical properties of oceanic waters: A reappraisal, *J. Geophys. Res.*, *106*, 7163–7180.

Morel, A., D. Antoine, and B. Gentili (2002), Bidirectional reflectance of oceanic waters: accounting for Raman emission and varying particle scattering phase function, *Appl. Opt.*, *41*, 6289–6306.

Morel, A., H. Claustre, D. Antoine, and B. Gentili (2007a), Natural variability of bio-optical properties in Case 1 waters: Attenuation and reflectance within the visible and near-UV spectral domains, as observed in South Pacific and Mediterranean waters, *Biogeosciences*, *4*, 913–925.

Morel, A., B. Gentili, H. Claustre, A. Babin, A. Bricaud, J. Ras, and F. Tieche (2007b), Optical properties of the ''clearest'' natural waters, *Limnol. Oceanogr.*, *52*, 217–229.

Morel, A., Y. Huot, B. Gentili, P. J. Werdell, S. B. Hooker, and B. A. Franz (2007c), Examining the consistency of products derived from various ocean color sensors in open ocean (Case 1) waters in the perspective of a multi-sensor approach, *Remote Sens. Environ.*, *111*, 69–88.

Mueller, J. L., and C. C. Trees (Eds.) (1997), *Revised SeaWiFS Prelaunch Algorithm for Diffuse Attenuation Coefficient K(490)*, NASA Goddard Space Flight Cent., Greenbelt, Md.

Mueller, J. L., G. S. Fargion, and C. R. McClain (2003), *Ocean Optics Protocols for Satellite Ocean Color Sensor Validation, Revision 4*, NASA Goddard Space Flight Cent., Greenbelt, Md.

O'Reilly, J., S. Maritorena, B. G. Mitchell, D. Siegel, K. L. Carder, S. Garver, M. Kahru, and C. McClain (1998), Ocean color chlorophyll algorithms for SeaWiFS, *J. Geophys. Res.*, *103*, 24937–24953.

Paulson, C. A., and J. J. Simpson (1977), Irradiance measurements in the upper ocean, *J. Phys. Oceanogr.*, *7*, 953–956.

Pegau, W. S., D. Gray, and J. R. V. Zaneveld (1997), Absorption and attenuation of visible and near-infrared light in water: Dependence on temperature and salinity, *Appl. Opt.*, *36*, 6035–6046.

Petzold, T. J. (1972), *Volume Scattering Functions for Selected Natural Waters*, pp. 72–78, Scripps Inst. of Oceanogr., La Jolla, Calif.

Platt, T., S. Sathyendranath, C. M. Caverhill, and M. Lewis (1988), Ocean primary production and available light: Further algorithms for remote sensing, *Deep Sea Res.*, *35*, 855–879.

Pope, R., and E. Fry (1997), Absorption spectrum (380–700 nm) of pure waters: II. Integrating cavity measurements, *Appl. Opt.*, *36*, 8710–8723.

Preisendorfer, R. W. (1976), *Hydrologic Optics*, vol. *1*, Introduction, Environ. Res. Lab., NOAA, U.S. Dep. of Commer., Honolulu, Hawaii.

Ryther, J. H. (1956), Photosynthesis in the ocean as a function of light intensity, *Limnol. Oceanogr.*, *1*, 61–70.

Sathyendranath, S., and T. Platt (1997), Analytic model of ocean color, *Appl. Opt.*, *36*, 2620–2629.

Sathyendranath, S., and T. Platt (2007), Spectral effects in bio-optical control on the ocean system, *Oceanologia*, *49*, 5–39.

Sathyendranath, S., L. Lazzara, and L. Prieur (1987), Variations in the spectral values of specific absorption of phytoplankton, *Limnol. Oceanogr.*, *32*, 403–415.

Sathyendranath, S., A. D. Gouveia, S. R. Shetye, P. Ravindran, and T. Platt (1991), Biological control of surface temperature in the Arabian Sea, *Nature*, *349*, 54–56.

Shang, S., Z. Lee, and G. Wei (2010), Characterization of satellite-derived euphotic zone depth: Results for the China Sea, *Remote Sens. Environ.*, *115*, 180–186.

Shick, J. M., M. P. Lesser, and P. L. Jokiel (1996), Effects of ultraviolet radiation on corals and other coral reef organisms, *Global Change Biol.*, *2*, 527–545.

Siegel, D., J. C. Ohlmann, L. Washburn, R. R. Bidigare, C. T. Nosse, E. Fields, and Y. Zhou (1995), Solar radiation, phytoplankton pigments and radiant heating of the equatorial Pacific warm pool, *J. Geophys. Res.*, *100*, 4885–4891.

Sinha, R. P., and D. P. Häder (2002), Life under solar UV radiation in aquatic organisms, *Adv. Space Res.*, *30*, 1547–1556.

Smith, R. C., and J. J. Cullen (1995), Effects of UV radiation on phytoplankton, *Rev. Geophys.*, *33*, 1211–1223.

Smyth, T. J. (2011), Penetration of UV irradiance into the global ocean, *J. Geophys. Res.*, *116*, C11020, doi:10.1029/2011JC007183.

Stavn, R. H., and A. D. Weidemann (1988), Optical modeling of clear ocean light fields: Raman scattering effects, *Appl. Opt.*, *27*, 4002–4011.

Stavn, R. H., and A. D. Weidemann (1989), Shape factors, two-flow models, and the problem of irradiance inversion in estimating optical parameters, *Limnol. Oceanogr.*, *34*, 1426–1441.

Sullivan, J. M., and M. S. Twardowski (2009), Angular shape of the oceanic particulate volume scattering function in the backward direction, *Appl. Opt.*, *48*, 6811–6819.

Tedetti, M., and R. Sempere (2006), Penetration of ultraviolet radiation in the marine environment. A review, *Photochem. Photobiol.*, *82*, 389–397.

Twardowski, M. S., and P. L. Donaghay (2002), Photobleaching of aquatic dissolved materials: Absorption removal, spectral alteration, and their interrelationship, *J. Geophys. Res.*, *107*(C8), 3091, doi:10.1029/1999JC000281.

Vasilkov, A., N. Krotkov, J. Herman, C. McClain, K. Arrigo, and W. Robinsons (2001), Global mapping of underwater UV irradiances and DNA-weighted exposures using Total Ozone Mapping Spectrometer and Seaviewing Wide Field-of-view Sensor data products, *J. Geophys. Res.*, *106*, 27,205–227,219.

Vasilkov, A. P., J. Herman, N. A. Krotkov, M. Kahru, B. G. Mitchell, and C. Hsu (2002), Problems in assessment of the ultraviolet penetration into natural waters from space-based measurements, *Opt. Eng.*, *41*, 3019–3027.

Wang, M., S. Son, and L. W. Harding (2009), Retrieval of diffuse attenuation coefficient in the Chesapeake Bay and turbid ocean regions for satellite ocean color applications, *J. Geophys. Res.*, *114*, C10011, doi:10.1029/2009JC005286.

Werdell, P. J., and S. W. Bailey (2005), An improved bio-optical data set for ocean color algorithm development and satellite data product validation, *Remote Sens. Environ.*, *98*, 122–140.

Westberry, T. K., E. Boss, and Z.-P. Lee (2013), Influence of Raman scattering on ocean color inversion models, *Appl. Opt.*, *52*, 5552–5561.

Williamson, C. E., R. S. Stemberger, D. P. Morris, T. M. Frost, and S. G. Paulsen (1996), Ultraviolet radiation in North American lakes: Attenuation estimates from DOC measurements and implications for plankton communities, *Limnol. Oceanogr.*, *41*, 1024–1034.

Zaneveld, J. R. V., J. C. Kitchen, and H. Pak (1981), The influence of optical water type on the heating rate of a constant depth mixed layer, *J. Geophys. Res.*, *86*, 6426–6428.

Zepp, R., D. Erickson Iii, N. Paul, and B. Sulzberger (2006), Interactive effects of solar UV radiation and climate change on biogeochemical cycling, *Photochem. Photobiol. Sci.*, *6*(3), 286–300.

Zepp, R. G., G. C. Shank, E. Stabenau, K. W. Patterson, M. Cyterski, W. Fisher, E. Bartels, and S. L. Anderson (2008), Spatial and temporal variability of solar ultraviolet exposure of coral assemblages in the Florida Keys: Importance of colored dissolved organic matter, *Limnol. Oceanogr.*, *53*, 1909–1922.

Zhang, X. D., and L. B. Hu (2009), Estimating scattering of pure water from density fluctuation of the refractive index, *Opt. Express*, *17*, 1671–1678.

Zhao, J., B. Barnes, N. Melo, D. English, B. Lapointe, F. Muller-Karger, B. Schaeffer, and C. Hu (2013), Assessment of satellite-derived diffuse attenuation coefficients and euphotic depths in south Florida coastal waters, *Remote Sens. Environ.*, *131*, 38–50.

Zibordi, G., J.-F. Berthon, F. Mélin, D. D'Alimonte, and S. Kaitala (2009), Validation of satellite ocean color primary products at optically complex coastal sites: Northern Adriatic Sea, Northern Baltic Proper and Gulf of Finland, *Remote Sens. Environ.*, *113*, 2574–2591.